Hierarchical chestnut-like $MnCo_2O_4$ nanoneedles grown on nickel foam as binder-free electrode for high energy density asymmetric supercapacitors

Kwun Nam Hui [a, *], Kwan San Hui [b, **], Zikang Tang [a], V. V. Jadhav [c], Qi Xun Xia [c]

[a] Institute of Applied Physics and Materials Engineering, University of Macau, Avenida da Universidade, Taipa, Macau, China

[b] School of Mathematics, University of East Anglia, Norwich, NR4 7TJ, United Kingdom

[c] School of Materials Science and Engineering, Pusan National University, San 30 Jangjeon-dong, Geumjeong-gu, Busan 609-735, Republic of Korea

*Corresponding author.

E-mail: bizhui@umac.mo *(K. N. Hui)*

**Corresponding author.

E-mail: *k.hui@uea.ac.uk* *(K.S. Hui)*

ABSTRACT

Hierarchical chestnut-like manganese cobalt oxide ($MnCo_2O_4$) nanoneedles (NNs) are successfully grown on nickel foam using a facile and cost-effective hydrothermal method. High resolution TEM image further verifies that the chestnut-like structure is assembled by numerous 1D nanoneedles, which are formed by numerous interconnected $MnCo_2O_4$ nanoparticles with grain diameter of ~10 nm. The $MnCo_2O_4$ electrode exhibits high specific capacitance of 1535 F g^{-1} at 1 A g^{-1} and good rate capability (950 F g^{-1} at 10 A g^{-1}) in a 6 M KOH electrolyte. An asymmetric supercapacitor is fabricated using $MnCo_2O_4$ NNs on Ni foam (NF) as the positive electrode and graphene/NF as the negative electrode. The device shows an operation voltage of 1.5 V and delivers a high energy density of ~60.4 Wh kg^{-1} at a power density of ~375 W kg^{-1}. Moreover, the device exhibits an excellent cycling stability of 94.3% capacitance retention after 12000 cycles at 30 A g^{-1}. This work demonstrates that hierarchical chestnut-like $MnCo_2O_4$ NNs could be a promising electrode for the high performance energy storage devices.

KEYWORDS

$MnCo_2O_4$; Nanoneedles; Graphene; Hydrothermal; Asymmetric supercapacitor

1. INTRODUCTION

The fast-growing market for portable electronic devices and hybrid electric vehicles has highlighted the urgent need to develop portable, efficient and cost-effective energy storage devices [1-3]. Supercapacitors are the promising energy storage devices that can bridge the gap between batteries and conventional capacitors owing to high energy density, outstanding power density, long life span, excellent fast charge/discharge rate [4, 5]. Accordingly, supercapacitors have been

widely envisaged in mobile electrical systems, consumer electronics, energy management, and memory back-up systems [6, 7]. To date, there has been considerable interest in developing high energy supercapacitors that consisting of transition metal oxide electrodes as positive electrodes and carbonaceous electrodes as negative electrodes owing to their high specific capacitance and wider potential windows [8-10]. Among the reported metal oxides, cobalt-based spinel structure with the general formula, $A_xB_{3-x}O_4$, where A and B are two different transition metals of Co, Mn, and Ni types [11, 12], have demonstrated superior electrochemical storage properties, which is attributed to richer redox reaction properties and higher electronic conductivity compared to binary metal oxides. In particular, $MnCo_2O_4$ spinel structure has drawn extensive attentions in energy storage such as supercapacitor and Li-ion battery owing to its highest theoretical specific capacitance among other cobalt-based spinel structure [13], high specific capacitance, high rate capability, natural abundance, low cost, and environmental friendliness [14-19]. For example, Li et al. reported $MnCo_2O_4$ nanowire arrays as the electrode materials for supercapacitors and Li-ion batteries, which exhibited a noticeable improved capacitance of 349.8 F g^{-1} at 1 A g^{-1} and high specific discharge capacity of 1288.6 mA h g^{-1} at 100 mA g^{-1} [20]. Xu et al. synthesized porous $MnCo_2O_4$ nanowires as electrode for supercapacitor, which exhibited a remarkable specific capacitance of 1342 F g^{-1} at 1 A g^{-1} [21]. However, it is still challenging to obtain high energy density in $MnCo_2O_4$ systems [22, 23].

Here we report hierarchical chestnut-like $MnCo_2O_4$ nanoneedles (NNs) grown on nickel foam as a binder-free supercapacitor electrode using a facile hydrothermal method. $MnCo_2O_4$ NNs electrodes delivered an unprecedented high capacitance of 1535 F g^{-1} at 1 A g^{-1} with an outstanding rate capability (83.3% capacity retention at 10 A g^{-1}) in a 6 M KOH electrolyte. An asymmetric supercapacitor (ASC) with operating potential at 1.5 V was assembled with the chestnut-like

$MnCo_2O_4$ NNs on nickel foam (NF) as the positive electrode and graphene/NF as the negative electrode. The ASC device showed a high energy density of ~60.4 Wh kg^{-1} at a power density of ~375 W kg^{-1}. Moreover, the device demonstrated excellent cycling stability with 94.3% capacitance retention after 12000 cycles at 30 A g^{-1} in a 6 M KOH electrolyte.

2. EXPERIMENTAL METHODS:

Synthesis of spinel $MnCo_2O_4$ nanoneedles on Ni foam

All the reagents used in the experiment were of analytical grade and used as received. The spinel $MnCo_2O_4$ NNs electrodes were prepared using a simple hydrothermal method. In a typical synthesis process, 0.02 M manganese nitrate ($Mn(NO_3)_2 \cdot 4H_2O$), 0.04 M cobalt nitrate, 0.12 M ammonium fluoride (NH_4F), and 0.24 M urea ($CO(NH_2)_2$) were added to 80 ml of water and transferred to an autoclave. Ni foam (NF; 10 mm x 50 mm x 0.1 mm; 110 ppi (pores per inch); mass density 320 g/m^2; Artenano Company Limited, Hong Kong) was pretreated sequentially with acetone, 2 M HCl solution, deionized (DI) water, and ethanol, for 15 min each to ensure a clean surface. The cleaned NF was then added and the resulting mixture was heated to 100 °C for 5 h. After the reaction was complete, the autoclave was allowed to cool naturally to room temperature. The samples were washed, dried and then treated thermally at 300 °C for 2h to obtain $MnCo_2O_4$ NNs. The active mass of $MnCo_2O_4$ was weighted by a semi-micro balance (Precisa, XR205SM-DR) with a readability of 0.01 mg. The loading mass of $MnCo_2O_4$ NNs on NF was approximately 1.1 mg cm^{-2}.

Preparation of graphene/NF as negative electrode

Graphite oxide (GO) was prepared from graphite powder using a modified Hummers method as published previously [24, 25]. The graphene was prepared by applying thermal expansion of the as-fabricated GO powder at 1050 ºC for 30 s in an Ar atmosphere [26]. The graphene electrode was prepared according to our previous work [27]. Briefly, 85 wt% of graphene was mixed with 10 wt% acetylene black and 5 wt% polytetrfluoroethylene (PTFE), and a small amount of water. Then resulting mixture was coated onto the nickel foam (1 cm × 1 cm). After pressing under a pressure of 20 MPa, the electrode was dried at 80 ºC overnight in a vacuum oven. The mass loading for graphene electrode was determined by comparing the mass difference between the original NF and the NF coated with mixture. The loading mass of the graphene on NF was approximately 5 mg cm^{-2}.

Material characterizations

The phase of the synthesized electrode was examined by X-ray diffraction (XRD, D8-Discovery Bruker) using Cu Kα radiation (λ=1.54 Å) at an accelerating voltage and current of 40 kV and 200 mA, respectively. The XRD pattern was recorded over the 20~80° (2θ) range at a scanning speed of 0.2 °/s. The microstructure and morphology were confirmed by field-emission scanning electron microscopy (SEM, Hitachi S-4800) and high resolution transmission electron microscopy (TEM, JEOL, JEM-2010F). The valence state of the prepared samples was determined by X-ray photoelectron spectroscopy (XPS, VG Scientifics ESCALAB250), which was calibrated to the carbon C 1s peak at 284.6 eV.

Electrochemical characterizations

Cyclic voltammetry (CV), galvanostatic charge/discharge (GCD) tests and electrochemical impedance spectroscopy (EIS) were obtained using an electrochemical workstation system (nSTAT, IVIUM). All electrochemical measurements were carried out in a conventional three-electrode system with a 6 M KOH aqueous electrolyte at room temperature. Platinum foil and Hg/Hg_2Cl_2 (standard calomel electrode, SCE) were used as the counter and reference electrodes, respectively. CV tests were measured between 0 and 0.6 V (vs. SCE) at various scan rates. GCD meassurements were performed in the potential range between 0 to 0.6 V (vs. SCE) at different current densities. Cycle stability tests of the $MnCo_2O_4$ NNs/NF electrode was measured at 5 A g^{-1} for 2500 cycles, while the cycling stability of $MnCo_2O_4$ NNs//G asymmetric supercapacitor device was measured at 30 A g^{-1} for 12000 cycles. The EIS data was collected over the frequency range from 100 kHz to 0.01 Hz at the open circuit potential with an AC perturbation of 5 mV.

The specific capacitance (C_s) was calculated using the following equation [28]:

$$C_s = \frac{I \times \Delta t}{m \times \Delta V} \qquad (1)$$

where I (A) is the constant discharge current, Δt (s) is the discharge time, ΔV (V) is the voltage drop upon discharging (excluding the IR drop), and m (g) is the mass of the active materials.

***Fabrication of $MnCo_2O_4$ NNs//graphene* asymmetric supercapacitor**

To fabricate the ASC device, chestnut-like $MnCo_2O_4$ NNs/NF and graphene/NF were used as the positive and negative electrodes, respectively. Based on the three-electrode electrochemical measurement results of both $MnCo_2O_4$ NNs and graphene electrodes, cell balance was achieved by setting the electrode mass ratio of cathode/anode to 0.18 (the anode loading mass is around 7.2 mg cm^{-2}). The G/NF electrode was pressed and combined with $MnCo_2O_4$ NNs/NF electrode using

a piece of polypropylene paper and 6.0 M KOH as the separator and electrolyte, respectively, to assemble the CR2302 cell.

For charge balance of the ASCs, the voltammetric charges of the positive electrode and the negative electrode followed the equation, $q_+ = q_-$. The voltammetric charges (q) were estimated using the following equation [29]:

$$q = C \times \Delta V \times m \qquad (2)$$

where C_s is the specific capacitance (F g^{-1}) of each electrode, ΔV is the potential window (V) of each electrode and m is the mass loading (g) of each electrode. Therefore, the mass ratio of the positive and negative electrodes followed the equation,

$$\frac{m_+}{m_-} = \frac{C_- \times \Delta V_-}{C_+ \times \Delta V_+} \qquad (3)$$

The energy density E (Wh kg^{-1}) and power density P (W kg^{-1}) were calculated as follows:

$$E = 0.5 \times C_s \times \Delta V \qquad (4)$$

$$P = E/\Delta t \qquad (5)$$

where C_s is the specific capacitance (F g^{-1}), ΔV is the potential range (V) and Δt is the discharge time (s).

3. RESULTS AND DISCUSSION

Fig. 1a presents the XRD pattern of $MnCo_2O_4$ NNs powder scratched from NF after air calcination at 300 °C for 2h. All XRD peaks were indexed to the (111), (220), (311), (400), (422), (511), and (440) crystal planes of pure cubic spinel $MnCo_2O_4$, which is in agreement with the standard values (JCPDS card no. 23-1237) [30]. No other phases were observed, suggesting that all the XRD peaks could be assigned to a well-crystallized $MnCo_2O_4$ spinel structure. The structure of the $MnCo_2O_4$ NNs is regarded as a mixed valence oxide that adopts a cubic spinel structure, in which manganese

(Mn) and cobalt (Co) might be distributed over both octahedral and tetrahedral sites [31, 32]. Fig. 1b-d show SEM images of the $MnCo_2O_4$ NNs grown on the NF. Fig. 1b-c show a hierarchical chestnut-like morphology of $MnCo_2O_4$ microspheres with mean diameter of 5 µm covering completely the NF. Fig. 1b reveals $MnCo_2O_4$ microspheres are composed of numerous thin and long nanoneedles grown vertically outward from the center, forming an open porous network structure that can provide abundant porous surface area between the electrode and electrolyte. A chestnut fruit picture is shown in the inset of Fig. 1b. Fig. 1c shows the high magnified SEM image of a $MnCo_2O_4$ microsphere where well-resolved nanoneedles were clearly observed. Each nanoneedle is rounded in shape with 19 nm in tip diameter and 50 nm in bottom diameter as shown in Fig. 1d. These unique nanoneedle structures form an open porous network which can facilitate the charge transport and rapid ion diffusion [33], which is beneficial to superior electrochemical reaction.

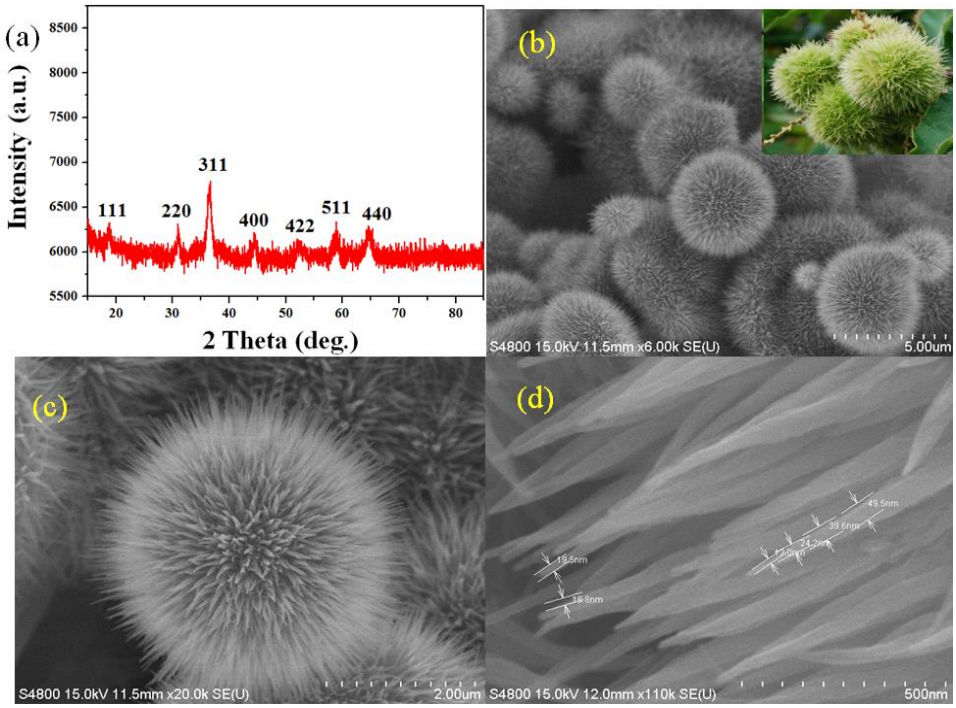

Fig. 1. (a) XRD pattern and (b-d) FESEM images of $MnCo_2O_4$ nanoneedles microspheres. The inset in (b) is the chestnut fruit photo.

The morphology and microstructure of the $MnCo_2O_4$ nanoneedle microspheres were further examined by TEM. Fig. 2a shows the TEM image of a $MnCo_2O_4$ nanoneedle microsphere having a chestnut-like structure. High resolution TEM image further verifies that the chestnut-like structure is assembled by numerous 1D nanoneedles, which is formed by numerous interconnected $MnCo_2O_4$ nanoparticles with grain diameter of ~10 nm (Fig. 2b). The porous characteristic of 1D nanoneedles enables efficient and rapid diffusion of electrolyte ions to electroactive surface sites for Faradaic reaction, leading to high specific capacitance [34]. Fig. 2c shows the lattice fringes with equal interplanar distance of 0.296 nm, 0.252 nm, and 0.212 nm, which correspond to the (220), (311), and (400) planes of cubic $MnCo_2O_4$, further confirming the formation of polycrystalline $MnCo_2O_4$ nanoneedles [35]. EDS mapping analysis of the nanoneedle bundles further confirmed the formation of $MnCo_2O_4$ (Fig. 2d).

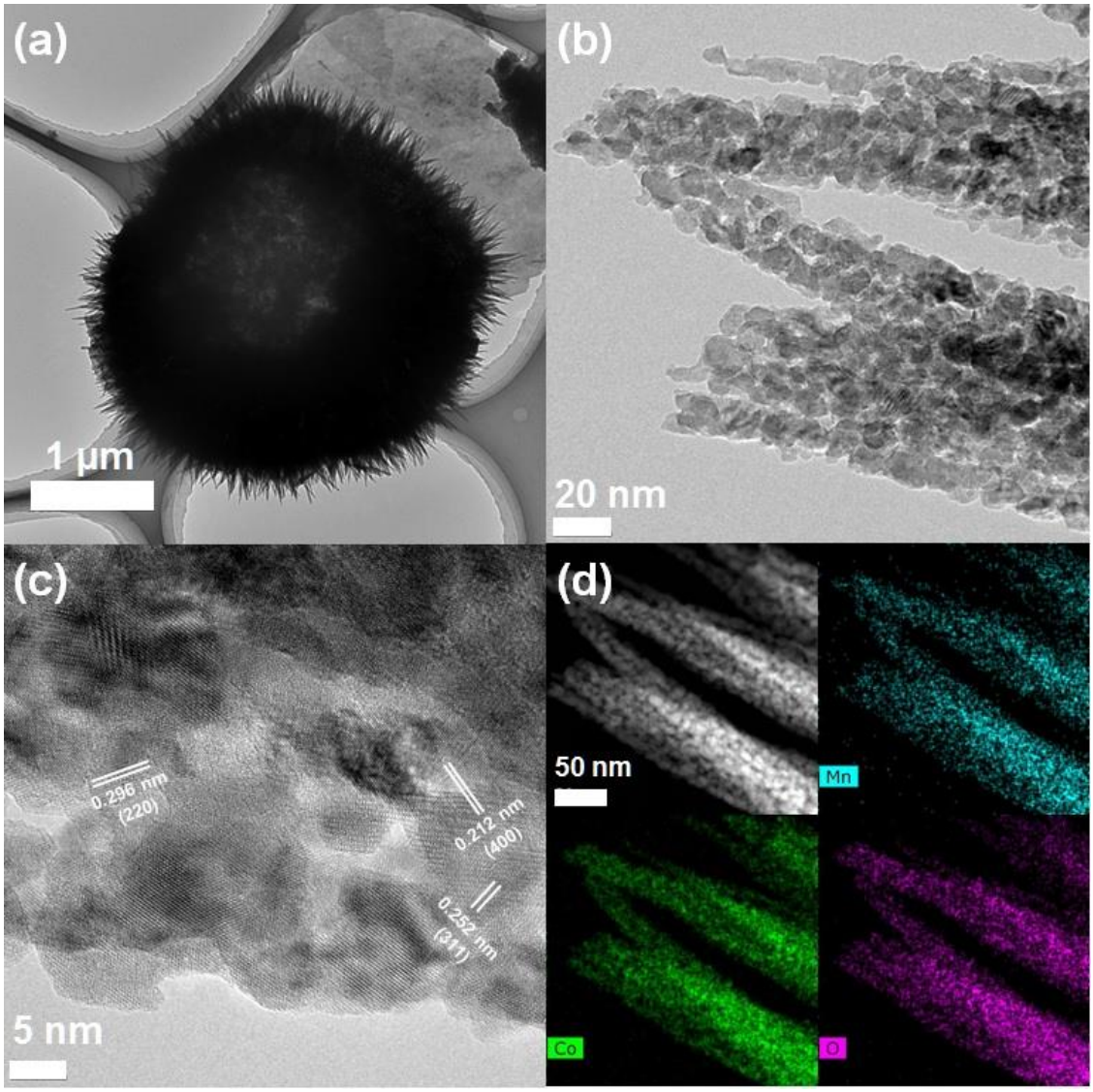

Fig. 2. (a) TEM images of a $MnCo_2O_4$ nanoneedle microsphere. (b-c) HRTEM image of $MnCo_2O_4$ nanoneedles. (d) dark-field scanning TEM image of $MnCo_2O_4$ nanoneedle and the corresponding EDS mapping of Mn, Co, and O.

The elemental composition and oxidation valance state of $MnCo_2O_4$ NNs were characterized by XPS. Fig. 3a shows the typical signals of Mn_{2p}, Co_{2p}, O_{1s} core levels from the spectrum, confirming the presence of Mn, Co, and O. As shown in Fig. 3b, two types of manganese species were detected and attributed to species containing Mn^{2+} and Mn^{3+} ions. The Mn 2p spectrum shows a Mn $2p_{3/2}$ peak at ~ 642.5 eV and a Mn $2p_{1/2}$ peak at ~ 654 eV, corresponding to the Mn (II) and Mn (III),

respectively [29]. The Co 2p spectrum (Fig. 3c) opens a broad Co $2p_{3/2}$ peak at ~780.0 eV and a Co $2p_{1/2}$ peak at ~796.0 eV, indicating the coexistence of Co (II) and Co (III) [36]. The O 1s spectrum confirms the presence of oxygen in the spinel structure lattice (Fig. 3d). The high-resolution spectrum of the O 1s region reveals three oxygen contributions; O_1, O_2 and O_3. In particular, the O_1 component at ~529.7 eV is typical of metal-oxygen bonds [37]. The well-resolved O_2 component at ~531.2 eV is due to the larger number of defect sites with low oxygen coordination normally observed in materials with small particles [38]. The component O_3 at ~532.6 eV is attributed to the multiplicity of physi- and chemi-sorbed water at or near the surface [39]. Overall, the electron couples of Mn^{3+}/Mn^{2+}, Co^{3+}/Co^{2+} and O^{2-} coexist in the chestnut-like $MnCo_2O_4$ NNs structure, which provides a richer electrochemical activities for supercapacitor applications.

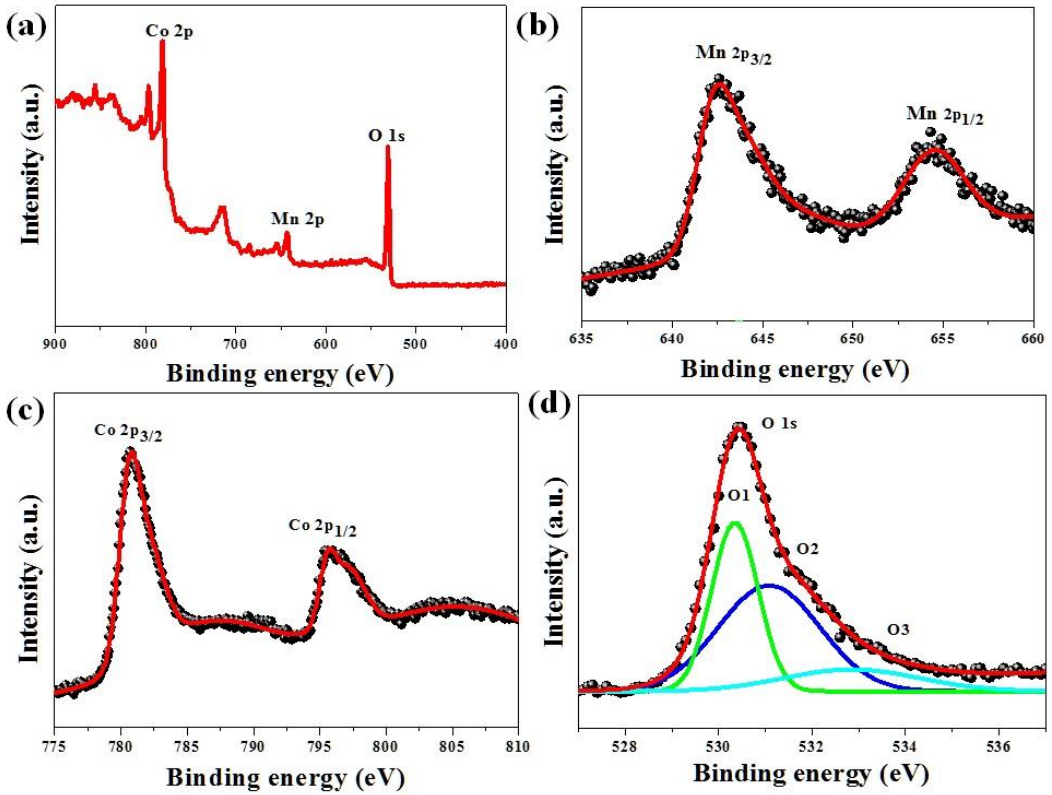

Fig. 3. (a) XPS survey spectrum, (b) Mn 2p, (c) Co 2p, and (d) O 1s spectra of $MNCo_2O_4$ NNs.

To evaluate the electrochemical properties of the $MnCo_2O_4$ NNs structure as superior electrode in supercapacitors, the CV curves of the $MnCo_2O_4$ NNs electrode was studied. To ensure the specific capacitance is contributed mainly from $MnCo_2O_4$ NNs material, CV data of the hydrothermal treated NF electrode without $MnCo_2O_4$ NNs loading was measured. Fig. 4a shows the electrochemical properties of the $MnCo_2O_4$ NNs electrode and hydrothermal treated NF electrode without $MnCo_2O_4$ NNs loading measured at various scan rates between 2 and 30 mVs^{-1} with potential window ranging from 0 to 0.6 V (vs. SCE) in a 6 M KOH solution. The CV curve of the hydrothermal treated Ni foam is a straight line, indicating the specific capacitance of the treated Ni foam is insignificance [27]. A pair of redox peaks is clearly observed in the CV curves of $MnCo_2O_4$ NNs electrode, which originates mainly from the reversible Faradaic redox reactions of Co^{2+}/Co^{3+} [14, 29]. With increasing scan rates, the current density increases and the positions of the anodic and cathodic peaks are shifted to a more anodic and cathodic direction, respectively, suggesting fast and reversible redox reactions occurring at the electrode/electrolyte interface [41]. With increasing the sweep rate from 2 mV s^{-1} to 20 mV s^{-1}, the position of the cathodic peaks shifts slightly from 0.46 V to 0.45 V, which indicates efficient electron conduction and ion transports of the $MnCo_2O_4$ NNs structure at higher scan rates. Fig. 4b presents the GCD curves of the $MnCo_2O_4$ NNs electrode within a 0−0.6 V voltage range at different current densities 1, 2, 3, 5, 8, and 10 A g^{-1}. All the curves are nonlinear and asymmetrical at different current densities, confirming the pseudocapacitive behavior in nature [42]. In addition, the charge/discharge curves are highly symmetrical without an obvious IR drop at various current densities, indicating a rapid I-V response and excellent electrochemical reversibility. The calculated specific capacitance (C_s) based on the discharge curves as a function of current density was plotted in Fig. 4c. The $MnCo_2O_4$ NNs electrode delivers C_s of 1535, 1366, 1295, 1116, 1002, and 950 F g^{-1} at current densities of 1,

2, 3, 5, 8, and 10 A g^{-1}, respectively, exhibiting 61.8% capacitance retention when the current density increased by a factor of 10 (from 1 A g^{-1} to 15 A g^{-1}). As the kinetics of the redox reactions is governed mainly by migration and diffusion of ions in the electrolyte, the diffusion and migration of electrolytic ions are suppressed at high current density [33, 43], thus resulting in inefficiency of the inner electroactive surface area for charge storage; consequently, smaller C_s is obtained. Nevertheless, the obtained result is superior to those reported for $MnCo_2O_4$ nanosheets (400 F g^{-1} at 1 A g^{-1}) [44], 1D $MnCo_2O_4$ nanowires and nanorods (349.8 F g^{-1} at 1 A g^{-1}; 328.9 F g^{-1} at 20 A g^{-1}) [20], spinel $MnCo_2O_4$ nanoparticle (405 F g^{-1} at 5 mA cm^{-2}) [45], porous $MnCo_2O_4$ nanowires (1342 F g^{-1} at 1 A g^{-1}) [32], and mesoporous $MnCo_2O_4$ nanoflakes (1487 F g^{-1} at 1 A g^{-1}) [46]. The cycle stability is a crucial parameter for practical supercapacitor applications. The cycle performance of the $MnCo_2O_4$ NNs electrode was explored at a current density of 5 A g^{-1}, as shown in Fig. 4d. After 2500 cycles, 83.8% of the capacitance is maintained. The inset in Fig. 4d shows the charge/discharge curves of the $MnCo_2O_4$ electrode at 1st and 2500th cycles. The superior electrochemical performance is attributed to the following merits of the proposed $MnCo_2O_4$ NNs structure. First, the 1D porous $MnCo_2O_4$ NNs structure is composed of numerous $MnCo_2O_4$ nanoparticles, thereby resulting in the more electroactive surface sites for electrochemical reactions, which leads to faster kinetics in electron and ion transportation [29]. Second, the chestnut-like $MnCo_2O_4$ structure was grown hierarchically on NF, which preserves the open network of individual chestnut-like structure, allowing easy access of electrolyte to the electroactive surface sites, hence facilitating ion diffusion at the electrode/electrolyte interface [41]. Third, the direct hydrothermal growth of hierarchical $MnCo_2O_4$ NNs structures on NF ensures good mechanical adhesions between $MnCo_2O_4$ structures and NF current collector, thus ensuing good electrical conductivity of the $MnCo_2O_4$ electrode [33].

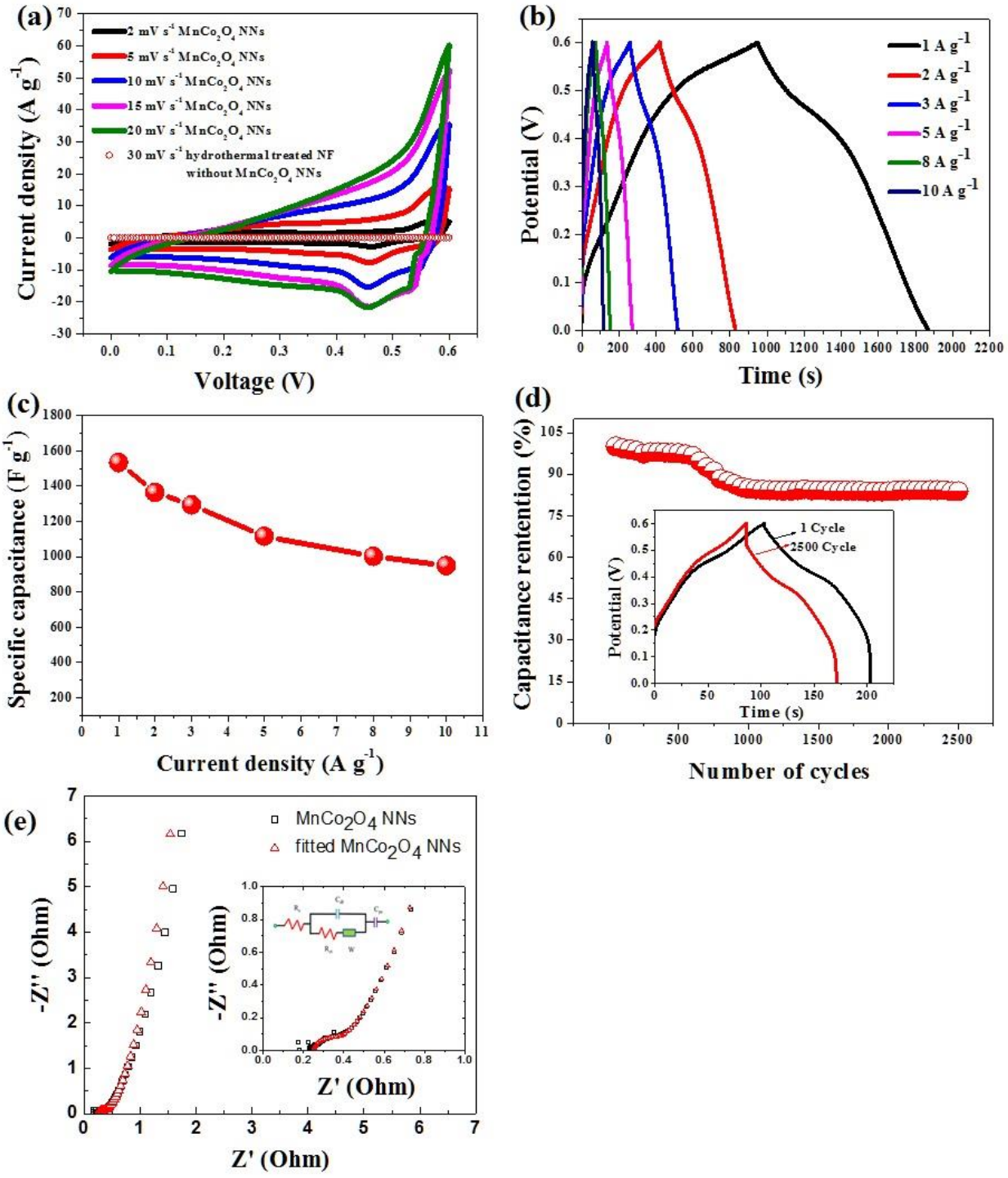

Fig. 4. (a) CV curves of $MnCo_2O_4$ NNs electrode and hydrothermal treated NF electrode without $MnCo_2O_4$ NNs loading at various scan rates from 2-30 mV s^{-1}. (b) Galvanostatic charge/discharge curves and (c) Specific capacitance of $MnCo_2O_4$ NNs electrode at current densities ranging from 1-10 A g^{-1}. (d) Cycling performance of $MnCo_2O_4$ NNs electrode at 5 A g^{-1}. (e) Nyquist plot of $MnCo_2O_4$ NNs electrode.

EIS is commonly used to examine the ion transport properties of electrode materials for supercapacitors. EIS was carried out to determine the charge transfer kinetics of the $MnCo_2O_4$ NNs structure. Fig. 4e shows the impedance Nyquist plot of the $MnCo_2O_4$ NNs electrode over the frequency range, 10 kHz to 0.01 Hz, at the open circuit potential in a 6 M KOH electrolyte. The bottom-right inset in Fig. 4e shows the proposed equivalent circuit for the measured impedance data, which involves the internal resistance (R_s), double-layer capacitance (C_{dl}) and Faradic charge transfer resistance (R_{ct}), a Warburg diffusion element (Z_w), and pseudocapacitance (C_F) [47, 48]. Equation 6 and 7 express the overall impedance, Z, of the equivalent circuit in the inset of Fig. 4e [49]:

$$Z = R_s + \frac{1}{j\omega C_{dl} + \frac{1}{R_{ct} + Z_w}} - j\frac{1}{\omega C_F} \quad \ldots (6)$$

$$Z_w = \frac{W}{\sqrt{j\omega}} \ldots (7)$$

where j is the imaginary unit, ω is the angular frequency (Hz) and W is the Warburg parameter in units of $\Omega\ s^{-1/2}$. This W parameter is an increasing function of the resistance for electrolyte transport in a porous electrode. At sufficiently high frequencies, the overall impedance can be reduced to Equation 8, corresponding to a locus showing a semicircle that intercepts the real axis at R_s and $R_s + R_{ct}$ in the Nyquist plot [50].

$$Z = R_s + \frac{1}{j\omega C_{dl} + \frac{1}{R_{ct}}} \ldots (8)$$

The high frequency intercept of the semicircle on the real axis shows the R_s, representing a combinational resistance of the electrode, bulk electrolyte, and the resistance at the interface between current collector and $MnCo_2O_4$ NNs materials. The diameter of the semicircle corresponds to the R_{ct} during electrochemical process. In low frequency region, the straight line with an angle at almost 45° with the real axis (Z') corresponds to the Z_w and is the result of the

frequency dependence of ion diffusion in the electrolyte [51]. The impedance parameters R_s, C_{dl}, R_{ct}, Z_w and C_F values calculated from the complex nonlinear least square fitting are shown in Table 1. Fig. 4e clearly shows that the $MnCo_2O_4$ NNs electrode has a low R_s (0.252 Ω). Moreover, the impedance spectrum of the $MnCo_2O_4$ NNs electrode reveals a small semicircle, which indicates a low R_{ct} (0.113 Ω) of the $MnCo_2O_4$ NNs electrode, thereby suggesting that the $MnCo_2O_4$ NNs electrode has a high electrochemical activity. These results are attributed to the porous feature of the 1D nanoneedles and interconnected open network of $MnCo_2O_4$ NNs architecture, which lead to an enhanced ionic diffusion and charge transport.

Table 1 EIS fitting parameters of $MnCo_2O_4$ NNs electrode

R_s (Ω)	R_{ct} (Ω)	C_{dl} (F)	W ($\Omega s^{-1/2}$)	C_F (F)
0.252	0.113	0.00395	2.39	3.2

The as-obtained G/NF electrode displays excellent electric double layer capacitance properties at -1.0-0.0 V (vs. SCE), as shown in Fig. 5a. The C_s of the G/NF electrode, which was calculated from its GCD curves (Fig. 5b), reaches 171 F g^{-1} at 1 A g^{-1} and 100 F g^{-1} at 20 A g^{-1} with a good retention rate of 58.4% (Fig. 5c), which is comparable to those reported previously for graphene-based supercapacitors [52, 53]. EIS fitted data reveals that G/NF has low R_s and R_{ct} values of 0.481 Ω and 0.723 Ω, respectively (Fig. 5d).

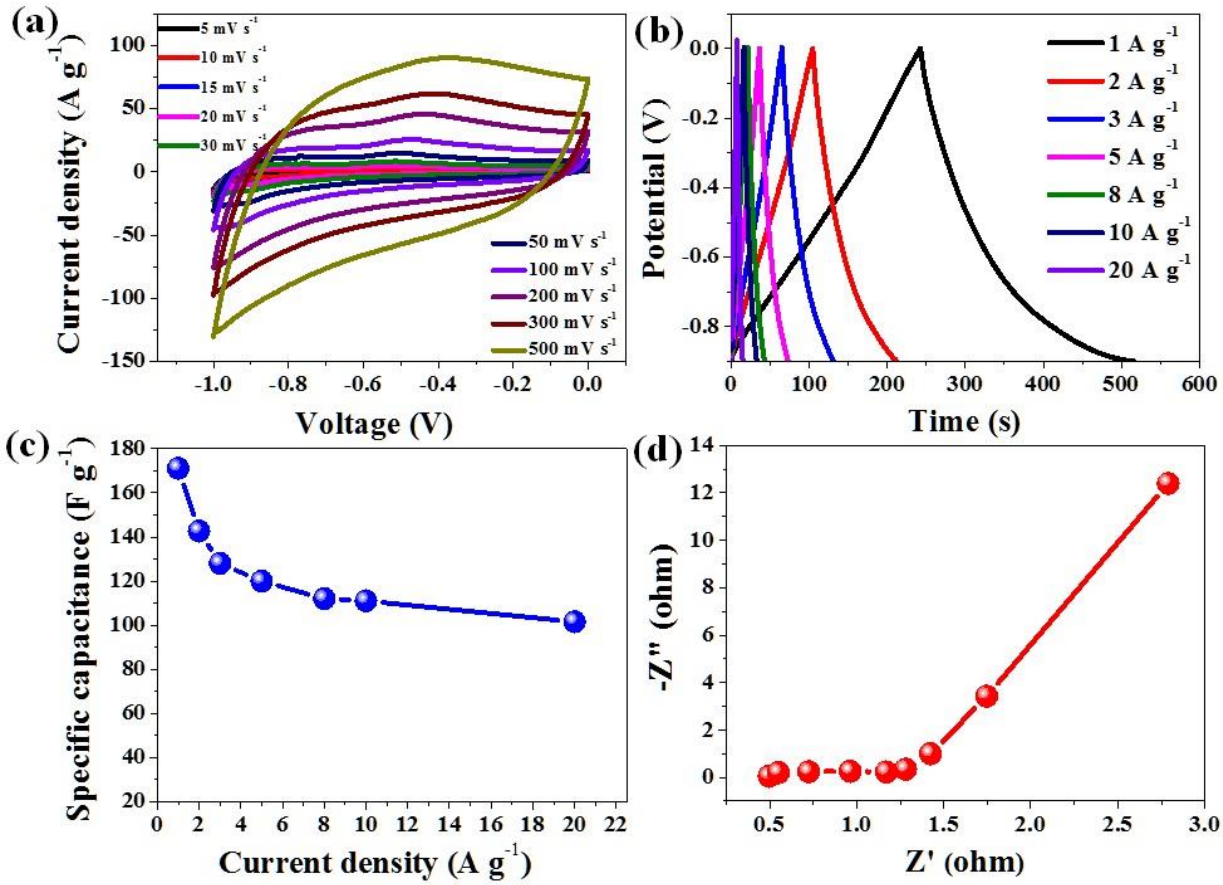

Fig. 5. (a) CV curves at different scan rates, (b) Galvanostatic charge/discharge curves, (c) Specific capacitance at different current densities, and (d) Nyquist plot of the G/NF electrode.

To evaluate the performance of the $MnCo_2O_4$ NNs//G in SC applications, an ASC was fabricated with $MnCo_2O_4$ NNs//G and G/NF as the positive and negative electrodes, respectively. Fig. 6a presents the CV curves of $MnCo_2O_4$ NNs//G ASC at different scan rates from 5 to 200 mV s^{-1} within a 0-1.6 V potential window. The ASC device shows a relatively quasi-rectangular CV shape with weak redox peaks, which indicates $MnCo_2O_4$//G ASC exhibiting good capacitive behavior with the combination of EDLC and pseudocapacitance. With the increase in scan rate from 5 to 200 mV s^{-1}, the shapes of the CV curves of the device do not change, implying the desirable rapid charge/discharge characteristic for supercapacitors. Fig. 6b shows the GCD curves of $MnCo_2O_4$//G ASC with cell voltage as high as 1.5 V at various current densities from 0.5 to 5 A g^{-1}. During the

charge/discharge steps, the charge curves of $MnCo_2O_4$//G ASC are almost symmetrical to its corresponding discharge counterpart, confirming the excellent electrochemical reversibility [37]. The C_s of the $MnCo_2O_4$ NNs//G ASC based on the total mass of the device was calculated from the charge/discharge curves according to eq. (1). The calculated C_s are 193.21, 176.88, 168, 153, 144, and 145 F g^{-1} at current densities of 0.5, 1, 1.5, 2.5, 4, and 5 A g^{-1}, respectively, as shown in Fig. 6c. The GCD test was carried out to evaluate the cycle stability of the $MnCo_2O_4$ NNs //G ASC for 12000 cycles at a current density of 30 A g^{-1}. As shown in Fig. 6d, the ASC device shows 94.3 % capacitance retention after 12000 cycles, revealing $MnCo_2O_4$ NNs structure as an excellent electrode material for supercapacitors. The inset in Fig. 6d shows the charge/discharge curves of the 1^{st}, 6000^{th}, and 12000^{th} cycle. Fig. 6e shows the impedance Nyquist plot of the ASC device. From the fitted EIS data, R_s and R_{ct} are 0.316 Ω and 0.297 Ω, respectively, indicating a very low internal resistance and charge transfer resistance of the $MnCo_2O_4$ NNs//G ASC. The energy and power densities were calculated to further demonstrate the electrochemical performance of the supercapacitors, as shown in the Ragone plot in Fig. 6f. Remarkably, the present device delivers a maximum energy density of about 60.4 Wh kg^{-1} at a power density of 375 W kg^{-1}. This energy density is significantly larger than those of spinel-based asymmetric supercapacitors reported to date, such as $NiCo_2O_4$//AC (15.4 Wh kg^{-1} at 375 W kg^{-1}) [54], $ZnCo_2O_4$//NGN-CNT (37.2 Wh kg^{-1} at 750 W kg^{-1}) [55], $ZnCo_2O_4$@MnO_2//α-Fe_2O_3 (37.8 Wh kg^{-1} at 648 W kg^{-1}) [56], and $CuCo_2O_4$ NRs//AC (42.8 Wh kg^{-1} at 15kW kg^{-1}) [57].

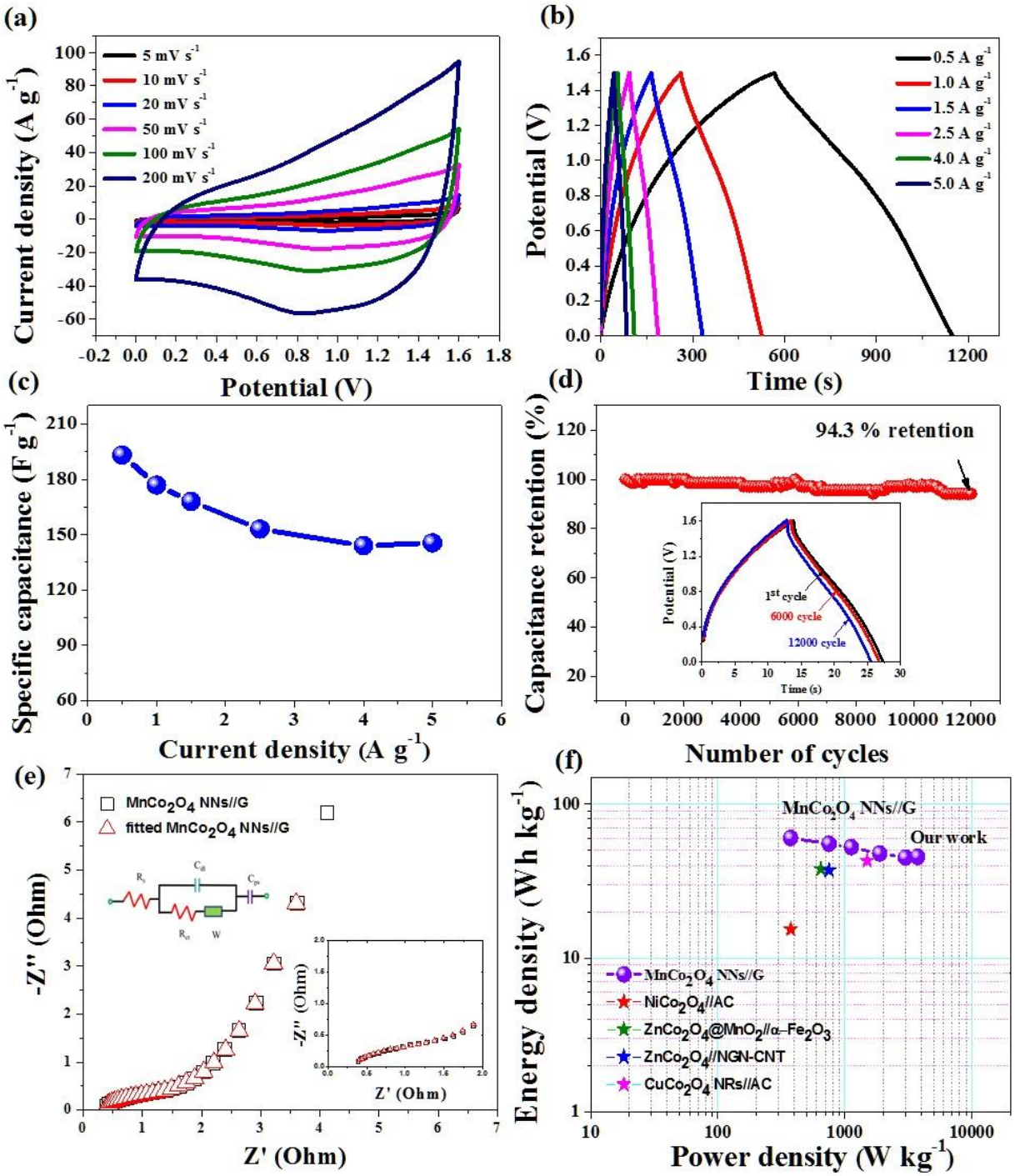

Fig. 6. Electrochemical characterization of the chestnut-like $MnCo_2O_4$ NNs//G asymmetric supercapacitor: (a) CV curves of the device at potentials between 0 to 1.6 V in a 6 M KOH electrolyte. (b) Galvanostatic charge/discharge measurements, (c) Specific capacitance of the device at different current densities. (d) Cycling performance of the device at 30 A g^{-1} for 12000 cycles. (e) Nyquist plot of the device. (f) Ragone plots of the energy and power density of the device as various charge/discharge rates.

Conclusions

Hierarchical chestnut-like $MnCo_2O_4$ NNs were grown on Ni foam using a facile and cost-effective hydrothermal method and tested as the positive electrode in an asymmetric supercapacitor with graphene as the negative electrode. The $MnCo_2O_4$ NNs electrode showed a specific capacitance of 1535 F g^{-1} at 1 A g^{-1} as well as excellent cycling stability with capacitance retention of approximately 83.3 % after 2500 cycles. The superior electrochemical performance of the hierarchical chestnut-like $MnCo_2O_4$ NNs electrode was attributed to its interconnected open-network of porous 1D $MnCo_2O_4$ NNs structure, which allows efficient electron transport and rapid ion diffusion at electroactive surface sites, as well as the facile permeation of the electrolyte into the active materials. The $MnCo_2O_4$ NNs//G ASC delivered a maximum energy density of 60.4 Wh kg^{-1} at a power density of 375 W kg^{-1} with an excellent cycle stability of 94.3% capacitance retention after 12000 cycles. Such hierarchical chestnut-like $MnCo_2O_4$ NNs structure would be a promising electrode material for high-performance energy storage devices.

Acknowledgements

This work was supported by the Basic Science Research Program through the National Research Foundation of Korea (NRF) funded by the Ministry of Education, Science and Technology (2014R1A1A2055740), Global Frontier Program through the Global Frontier Hybrid Interface Materials (GFHIM) program of the National Research Foundation of Korea (NRF) funded by the Ministry of Science, ICT & Future Planning (2013M3A6B1078874), the Science and Technology Development Fund from Macau SAR (FDCT-098/2015/A3), and the Start-up Research Grant (SRG2015-00057-FST) from Research & Development Office at University of Macau.

References

[1] H.S. Li, L.F. Shen, J. Wang, S. Fang, Y.X. Zhang, H. Dou, X.G. Zhang, J. Mater. Chem. A, 3 (2015) 16785-16790.

[2] X. Wang, Y. Zhang, C. Zhi, X. Wang, D. Tang, Y. Xu, Q. Weng, X. Jiang, M. Mitome, D. Golberg, Y. Bando, Nat. Comm., 4 (2013) 2905.

[3] P. Nie, L. Shen, G. Pang, Y. Zhu, G. Xu, Y. Qing, H. Dou, X. Zhang, J. Mater. Chem. A, 3 (2015) 16590-16597.

[4] L. Shen, L. Yu, H.B. Wu, X.-Y. Yu, X. Zhang, X.W. Lou, Nat. Commun., 6 (2015) 6694.

[5] X. Ren, C. Tian, S. Li, Y. Zhao, C.-A. Wang, Front. Mater. Sci., 9 (2015) 234-240.

[6] H. Jiang, L.P. Yang, C.Z. Li, C.Y. Yan, P.S. Lee, J. Ma, Energ. Environ. Sci., 4 (2011) 1813-1819.

[7] J.R. Miller, P. Simon, Science, 321 (2008) 651-652.

[8] X.C. Ren, C.L. Guo, L.Q. Xu, T.T. Li, L.F. Hou, Y.H. Wei, ACS Appl. Mater. Inter., 7 (2015) 19930-19940.

[9] S. Wang, B. Pei, X. Zhao, R.A.W. Dryfe, Nano Energy, 2 (2013) 530-536.

[10] W. Kong, C. Lu, W. Zhang, J. Pu, Z. Wang, J. Mater. Chem. A, 3 (2015) 12452-12460.

[11] Y.J. Zhai, H.Z. Mao, P. Liu, X.C. Ren, L.Q. Xu, Y.T. Qian, J. Mater. Chem. A, 3 (2015) 16142-16149.

[12] C.Z. Yuan, J.Y. Li, L.R. Hou, X.G. Zhang, L.F. Shen, X.W. Lou, Adv. Funct. Mater., 22 (2012) 4592-4597.

[13] S.G. Krishnan, M.V. Reddy, M. Harilal, B. Vidyadharan, I.I. Misnon, M.H. Ab Rahim, J. Ismail, R. Jose, Electrochim. Acta, 161 (2015) 312-321.

[14] S. Liu, K.S. Hui, K.N. Hui, ChemNanoMat, 1 (2015) 593-602.

[15] S. Yang, L. Zhi, K. Tang, X. Feng, J. Maier, K. Müllen, Adv. Funct. Mater., 22 (2012) 3634-3640.

[16] S.C. Ma, L.Q. Sun, L.N. Cong, X.G. Gao, C. Yao, X. Guo, L.H. Tai, P. Mei, Y.P. Zeng, H.M. Xie, R.S. Wang, J. Phys. Chem.. C, 117 (2013) 25890-25897.

[17] Z.Y. Sui, Y.N. Meng, P.W. Xiao, Z.Q. Zhao, Z.X. Wei, B.H. Han, ACS Appl. Mater. Inter., 7 (2015) 1431-1438.

[18] S.Q. Zhu, Q.L. Chen, Y.Y. Shi, Z.Y. Chen, R.Q. Bao. L. Zhou, L.R. Hou, K.N. Hui, C.Z. Yuan, J. Solid State Electrochem, 20 (2016) 713-723.

[19] F. Li, G. Li, H. Chen, J.Q. Jia, F. Dong, Y.B. Hu, Z.G. Shang, Y.X. Zhang, J. Power Sources, 296 (2015) 86-91.

[20] L. Li, Y.Q. Zhang, X.Y. Liu, S.J. Shi, X.Y. Zhao, H. Zhang, X. Ge, G.F. Cai, C.D. Gu, X.L. Wang, J.P. Tu, Electrochim. Acta, 116 (2014) 467-474.

[21] Y. Xu, X. Wang, C. An, Y. Wang, L. Jiao, H. Yuan, J. Mater. Chem. A, 2 (2014) 16480-16488.

[22] H. Xiaomin, W. Long, C. Xia, H. Yu, G. Caizhen, X. Ying, W. Ning, J. Mater. Chem. A, 2 (2014) 13103-13108.

[23] L. Ren, J. Chen, X. Wang, M. Zhi, J. Wu, X. Zhang, RSC Adv., 5 (2015) 30963-30969.

[24] L. Ren, K.S. Hui, K.N. Hui, J. Mater. Chem. A, 1 (2013) 5689-5694.

[25] L. Ren, K.N. Hui, K.S. Hui, Y.D. Liu, X. Qi, J.X. Zhong, Y. Du, J.P. Yang, Sci. Reps., 5 (2015) 14229.

[26] S. Zhang, J. Niu, H.H. Song, L.X. Zhu, J.S. Zhou, X.H. Chen, J.Z. Liu, S. Hong, R.R. Song, J. Mater. Chem. A, 1 (2013) 14103-14107.

[27] S.X. Wu, K.S. Hui, K.N. Hui, J. Phys. Chem. C, 119 (2015) 23358-23365.

[28] S. Liu, K.S. Hui, K.N. Hui, V.V. Jadhav, Q.X. Xia, J.M. Yun, Y.R. Cho, R.S. Mane, K.H. Kim, Electrochim. Acta, 188 (2016) 898-908.

[29] S. Liu, K.S. Hui, K.N. Hui, J.M. Yun, K.H. Kim, J. Mater. Chem. A, 4 (2016) 8061-8071.

[30] L. Li, Y.Q. Zhang, F. Shi, Y.J. Zhang, J.H. Zhang, C.D. Gu, X.L. Wang, J.P. Tu, ACS Appl. Mater. Inter., 6 (2014) 18040-18047.

[31] W.Y. Li, K.B. Xu, G.S. Song, X.Y. Zhou, R.J. Zou, J.M. Yang, Z.G. Chen, J.Q. Hu, Crystengcomm, 16 (2014) 2335-2339.

[32] Y.N. Xu, X.F. Wang, C.H. An, Y.J. Wang, L.F. Jiao, H.T. Yuan, J. Mater. Chem. A, 2 (2014) 16480-16488.

[33] L. Zhang, K.N. Hui, K.S. Hui, X. Chen, R. Chen, H. Lee, Int. J. Hydrogen Energy, 41 (2016) 9443-9453.

[34] S.X. Wu, K.S. Hui, K.N. Hui, K.H. Kim, J. Mater. Chem. A, 4 (2016) 9113-9123.

[35] P. Hao, Z.H. Zhao, L.Y. Li, C.C. Tuan, H.D. Li, Y.H. Sang, H.D. Jiang, C.P. Wong, H. Liu, Nanoscale, 7 (2015) 14401-14412.

[36] H. Hua, S.J. Liu, Z.Y. Chen, R.Q. Bao, Y.Y. Shi, L.R. Hou, G. Pang, K.N. Hui, X.G. Zhang, C.Z. Yuan, Sci. Reps., 6 (2016) 20973.

[37] Q.X. Xia, K.S. Hui, K.N. Hui, S.D. Kim, J.H. Lim, S.Y. Choi, L.J. Zhang, R.S. Mane, J.M. Yun, K.H. Kim, J. Mater. Chem. A, 3 (2015) 22102-22117.

[38] Y. Lei, J. Li, Y.Y. Wang, L. Gu, Y.F. Chang, H.Y. Yuan, D. Xiao, ACS Appl. Mater. Inter., 6 (2014) 1773-1780.

[39] S. Liu, K.S. Hui, K.N. Hui, ACS Appl. Mater. Inter., 8 (2016) 3258-3267.

[40] X.-F. Lu, D.-J. Wu, R.-Z. Li, Q. Li, S.-H. Ye, Y.-X. Tong, G.-R. Li, J. Mater. Chem. A, 2 (2014) 4706-4713.

[41] L.J. Zhang, J. Wang, J.J. Zhu, X.G. Zhang, K.S. Hui, K.N. Hui, J. Mater. Chem. A, 1 (2013) 9046-9053.

[42] L. Zhang, K.N. Hui, K.S. Hui, H. Lee, J. Power Sources, 318 (2016) 76-85.

[43] L. Zhang, K.N. Hui, K.S. Hui, H. Lee, Electrochim. Acta, 186 (2015) 522-529.

[44] T. Nguyen, M. Boudard, L. Rapenne, O. Chaix-Pluchery, M.J. Carmezim, M.F. Montemor, RSC Adv., 5 (2015) 27844-27852.

[45] L.B. Kong, C. Lu, M.C. Liu, Y.C. Luo, L. Kang, X.H. Li, F.C. Walsh, Electrochim. Acta, 115 (2014) 22-27.

[46] A.K. Mondal, D.W. Su, S.Q. Chen, A. Ung, H.S. Kim, G.X. Wang, Chem. Eur. J., 21 (2015) 1526-1532.

[47] O. Ghodbane, M. Louro, L. Coustan, A. Patru, F. Favier, J. Electrochem. Soc., 160 (2013) A2315-A2321.

[48] P. Sen, A. De, Electrochim. Acta, 55 (2010) 4677-4684.

[49] C.W. Huang, H.S. Teng, J. Electrochem. Soc., 155 (2008) A739-A744.

[50] K.P. Wang, H.S. Teng, J. Electrochem. Soc., 154 (2007) A993-A998.

[51] M.D. Stoller, S.J. Park, Y.W. Zhu, J.H. An, R.S. Ruoff, Nano Lett., 8 (2008) 3498-3502.

[52] Z.S. Wu, A. Winter, L. Chen, Y. Sun, A. Turchanin, X.L. Feng, K. Mullen, Adv. Mater., 24 (2012) 5130-5135.

[53] J.C. Huang, P.P. Xu, D.X. Cao, X.B. Zhou, S.N. Yang, Y.J. Li, G.L. Wang, J. Power Sources, 246 (2014) 371-376.

[54] X.F. Lu, D.J. Wu, R.Z. Li, Q. Li, S.H. Ye, Y.X. Tong, G.R. Li, J. Mater. Chem. A, 2 (2014) 4706-4713.

[55] W.L. Bai, H. Tong, Z.Z. Gao, S.H. Yue, S.C. Xing, S.Y. Dong, L.F. Shen, J.P. He, X.G. Zhang, Y.Y. Liang, J. Mater. Chem. A, 3 (2015) 21891-21898.

[56] W.Q. Ma, H.H. Nan, Z.X. Gu, B.Y. Geng, X.J. Zhang, J. Mater. Chem. A, 3 (2015) 5442-5448.

[57] A. Pendashteh, S.E. Moosavifard, M.S. Rahmanifar, Y. Wang, M.F. El-Kady, R.B. Kaner, M.F. Mousavi, Chem. Mater., 27 (2015) 3919-3926.

Figure Caption

Fig. 1. (a) XRD pattern and (b-d) FESEM images of $MnCo_2O_4$ nanoneedles microspheres. The inset in (b) is the chestnut fruit photo.

Fig. 2. (a) TEM images of a $MnCo_2O_4$ nanoneedle microsphere. (b-c) HRTEM image of $MnCo_2O_4$ nanoneedles. (d) dark-field scanning TEM image of $MnCo_2O_4$ nanoneedle and the corresponding EDS mapping of Mn, Co, and O.

Fig. 3. (a) XPS survey spectrum, (b) Mn 2p, (c) Co 2p, and (d) O 1s spectra of $MNCo_2O_4$ NNs.

Fig. 4. (a) CV curves of $MnCo_2O_4$ NNs electrode and hydrothermal treated NF electrode without $MnCo_2O_4$ NNs loading at various scan rates from 2-30 mV s^{-1}. (b) Galvanostatic charge/discharge curves and (c) Specific capacitance of $MnCo_2O_4$ NNs electrode at current densities ranging from 1-10 A g^{-1}. (d) Cycling performance of $MnCo_2O_4$ NNs electrode at 5 A g^{-1}. (e) Nyquist plot of $MnCo_2O_4$ NNs electrode.

Fig. 5. (a) CV curves at different scan rates, (b) Galvanostatic charge/discharge curves, (c) Specific capacitance at different current densities, and (d) Nyquist plot of the G/NF electrode.

Fig. 6. Electrochemical characterization of the chestnut-like $MnCo_2O_4$ NNs//G asymmetric supercapacitor: (a) CV curves of the device at potentials between 0 to 1.6 V in a 6 M KOH electrolyte. (b) Galvanostatic charge/discharge measurements, (c) Specific capacitance of the device at different current densities. (d) Cycling performance of the device at 30 A g^{-1} for 12000 cycles. (e) Nyquist plot of the device. (f) Ragone plots of the energy and power density of the device as various charge/discharge rates.

Table 1 EIS fitting parameters of $MnCo_2O_4$ NNs electrode